Available online at www.sciencedirect.com
ScienceDirect
Journal of Computational Physics 227 (2008) 6511–6531
JOURNAL OF COMPUTATIONAL PHYSICS
www.elsevier.com/locate/jcp

Prediction of cavitating flow noise by direct numerical simulation

Jung H. Seo [a], Young J. Moon [a,*], Byeong Rog Shin [b]

[a] Department of Mechanical Engineering, Korea University, Seoul 136-701, Republic of Korea
[b] Department of Mechanical Engineering, Changwon National University, Changwon 641-773, Republic of Korea

Received 26 April 2007; received in revised form 6 March 2008; accepted 11 March 2008
Available online 20 March 2008

Abstract

In this study, a direct numerical simulation procedure for the cavitating flow noise is presented. The compressible Navier–Stokes equations are written for the two-phase fluid, employing a density-based homogeneous equilibrium model with a linearly-combined equation of state. To resolve the linear and non-linear waves in the cavitating flow, a sixth-order compact central scheme is utilized with the selective spatial filtering technique. The present cavitation model and numerical methods are validated for two benchmark problems: linear wave convection and acoustic saturation in a bubbly flow. The cavitating flow noise is then computed for a 2D circular cylinder flow at Reynolds number based on a cylinder diameter, 200 and cavitation numbers, $\sigma = 0.7$–2. It is observed that, at cavitation numbers $\sigma = 1$ and 0.7, the cavitating flow and noise characteristics are significantly changed by the shock waves due to the coherent collapse of the cloud cavitation in the wake. To verify the present direct simulation and further analyze the sources of cavitation noise, an acoustic analogy based on a classical theory of Fitzpatrik and Strasberg is derived. The far-field noise predicted by direct simulation is well compared with that of acoustic analogy, and it also confirms the f^{-2} decaying rate in the spectrum, as predicted by the model of Fitzpatrik and Strasberg with the Rayleigh–Plesset equation.

Keywords: Cavitation noise; Cloud cavitation; Two-phase flow; Direct simulation

1. Introduction

Cavitation bubbles formed by a breakdown of cavitation sheet or collapse of vortex cavities are often responsible for the generation of loud noise and erosion damages, especially when they collapse coherently [1]. There have been some experimental works by Reisman et al. [2] and Levy et al. [3] to measure the cavitation noise with the sources identified. Cavitation experiments, especially for the cavitation noise, are,

* Corresponding author. Tel.: +82 2 3290 3358; fax: +82 2 926 9290.
E-mail address: yjmoon@korea.ac.kr (Y.J. Moon).

0021-9991/$ - see front matter © 2008 Elsevier Inc. All rights reserved.
doi:10.1016/j.jcp.2008.03.016

however, still quite difficult and numerical simulation is thereby important not only for the prediction but also as a means to investigate the flow physics.

Research on prediction of cavitating flow noise has been conducted for years but mostly for the fundamental cases. For example, a pressure pulse generated by oscillation of single bubble has been studied theoretically (and experimentally) by various researchers [4,5]. It is well-known that the acoustic pressure generated by the bubble can be scaled with the volume acceleration, an estimate of which can be derived from the Rayleigh's analysis [4]. For cloud of cavitation bubbles, Wang and Brennen [6,7] studied numerically the noise generated by the collapse of single cavitation cloud, by solving the Rayleigh–Plesset equation for the bubble dynamics and estimating the radiated noise with an analogy, i.e. volume acceleration of the cloud. Colonius et al. [8] also simulated the acoustic wave generation and propagation caused by wall oscillation in 1D bubbly cavitating flow. They used the model of van Wijngaarden [9], in which the equations of continuum two-phase flow are coupled with the micro-scale Rayleigh–Plesset equation.

The present study aims at direct numerical simulation of the cavitating flow noise. In order to simulate the cavitating flow, noise generation and its interactions with a body, the governing equations, cavitation model, and numerical methods should be carefully considered. For example, some classical interface tracking methods [10–12] cannot be used for cavitation noise simulation because the model cannot depict the detachment and collapse of the cavitation bubble – a core physics of cavitation noise. The group of homogeneous equilibrium models [13–20] could be the candidate because the models are capable of handling the bubble convection as well as the collapse. But most of these methods also are not suitable for the simulation of cavitation noise because the compressiblity effects of liquid and/or gas phase are not taken into account and the system of equations does not have the physical speed of sound as a characteristics.

In this regard, a density-based homogeneous equilibrium model [21] is employed. The governing equations are the compressible Navier–Stokes equations for the mixture fluid and the two-phase flow physics is treated by a linearly-combined equation of state to simulate the cavitating flow and the cavitation noise as well. The compressibility effect of liquid and gas phase are fully taken into account in the model. This density-based cavitation model is therefore very suitable for direct simulation of the cavitation noise because the governing equations are strictly in a hyperbolic system so that generation and propagation of the waves can be resolved with the high-order numerical schemes used in computational aero-acoustics (CAA).

Numerical schemes are also an important issue for direct simulation of cavitating flow noise. A numerical scheme should be able to capture the steep gradients of flow variables at Mach numbers varying from very low subsonic to supersonic, but for minimizing dispersion and dissipation errors, a high-order accuracy is also required to resolve the acoustic waves. With this respect, a second-order upwind TVD scheme widely used in simulation of cavitating flows [21] may be too dissipative. A high-order upwind scheme such as $r = 6$ WENO scheme [22] can be a proper shock-capturing scheme for this class but the scheme is sensitive and costly as well. Moreover, as for implementing the upwind scheme or the hybrid upwind/central scheme [23], the characteristics (i.e. eigenvalues and eigenvectors) of the two-phase mixture equations are not easily found for all cases.

In this study, a high-order central compact scheme with selective filtering technique is considered. The central compact scheme [24] widely used in CAA is efficient and high-order accurate but cannot capture the steep gradients such as shock waves because the scheme has no numerical diffusion. By the selective filtering based on the compact spatial-filtering schemes [25], the numerical diffusion can be controlled such that the selective filtering produces numerical diffusion only in the region where the steep gradients exist. This central compact scheme with selective filtering is effective and easy to apply to the present governing equations, as compared to other high-order upwind schemes [22,23].

In the present study, the cavitating flow noise from a 2D circular cylinder is computed by the proposed direct numerical simulation procedure, and the source mechanism and characteristics of the cavitation noise are examined for different cavitation numbers. The present article is organized as follows. In Section 2, a density-based homogeneous equilibrium model is introduced and the computational methods are presented in Section 3. Two validations on the cavitation model and numerical methods are performed in Section 4, and the computed results for the cavitation noise are presented in Section 5, with discussion on the noise generation mechanism and the sources. Finally, conclusions are summarized in Section 6.

2. Governing equations

2.1. Density-based homogenous equilibrium model

In the present study, a homogenous equilibrium model proposed by Shin et al. [21] is employed. In the homogenous medium, the mixture density ρ can be expressed by a linear combination of densities in the liquid-phase ρ_l and the gas-phase ρ_g as

$$\rho = (1-\alpha)\rho_l + \alpha\rho_g, \tag{1}$$

where α is a void fraction (gas volume fraction). The relation between the local void fraction α and the quality (gas mass fraction) Y is given by

$$\rho(1-Y) = (1-\alpha)\rho_l \quad \text{and} \quad \rho Y = \alpha\rho_g. \tag{2}$$

The equations of state for a pure liquid [26] and an ideal gas are written as

$$p + p_c = \rho_l K(T + T_c) \quad \text{for } Y = 0 \tag{3}$$

$$p = \rho_g RT \text{ for } Y = 1, \tag{4}$$

where p and T are the static pressure and temperature, p_c, T_c, K are the pressure, temperature, and liquid constant for the liquid state, and R is the gas constant. Using these two equations and the local equilibrium assumption, the equation of state, Eq. (1) for a locally homogenous gas–liquid two-phase medium can be written as

$$\rho = \frac{p(p+p_c)}{K(1-Y)p(T+T_c) + RY(p+p_c)T}. \tag{5}$$

The speed of sound for the isothermal condition at given mass fraction is derived as

$$c^2 = \frac{Y\{R(p+p_c) - Kp\} + Kp}{Y\{R(p+p_c)^2 - Kp^2\} - \rho KRY(1-Y)p_c T_c + Kp^2} \cdot \frac{p(p+p_c)}{\rho}, \tag{6}$$

by taking the mass fraction as a constant. The constants p_c, K and T_c for water in Eq. (5) were estimated as 1944.61 MPa, 472.27 J/kg K and 3837 K, respectively. The speed of sound estimated by Eq. (6) agrees well with the Karplus' experimental data at atmospheric pressure [21,27].

Based on the above mathematical modeling, which is under an isothermal condition and neglects the surface tension by assuming high Weber number condition ($We = \rho_0 u_0^2 l/S \gg 1$, where S is a surface tension and l is a length scale), the 2D governing equations for the mixture mass, momentum, and gas-phase mass conservation can be written as

$$\frac{\partial}{\partial t}\begin{pmatrix}\rho\\ \rho u\\ \rho v\\ \rho Y\end{pmatrix} + \frac{\partial}{\partial x}\begin{pmatrix}\rho u\\ \rho uu + p\\ \rho vu\\ \rho uY\end{pmatrix} + \frac{\partial}{\partial y}\begin{pmatrix}\rho v\\ \rho uv\\ \rho vv + p\\ \rho vY\end{pmatrix} = \frac{\partial}{\partial x}\begin{pmatrix}0\\ \tau_{xx}\\ \tau_{xy}\\ 0\end{pmatrix} + \frac{\partial}{\partial y}\begin{pmatrix}0\\ \tau_{xy}\\ \tau_{yy}\\ 0\end{pmatrix}. \tag{7}$$

The stress tensor τ and the mixture viscosity [28] μ can be expressed by

$$\tau_{xx} = \frac{2}{3}\mu\left(2\frac{\partial u}{\partial x} - \frac{\partial v}{\partial y}\right), \quad \tau_{yy} = \frac{2}{3}\mu\left(2\frac{\partial v}{\partial y} - \frac{\partial u}{\partial x}\right), \quad \tau_{xy} = \mu\left(\frac{\partial u}{\partial y} + \frac{\partial v}{\partial x}\right) \tag{8}$$

$$\mu = (1-\alpha)(1+2.5\alpha)\mu_l + \alpha\mu_g. \tag{9}$$

In cavitating flows, if local pressure drops under the vapor pressure then the liquid changes to vapor. This phase change is modeled by generation of quality Y in the homogeneous equilibrium model. The phase change is performed explicitly by Eqs. (1)–(5) with thermodynamic phase-interface condition after every iteration. In the present density-based method, following values are estimated to check the phase change:

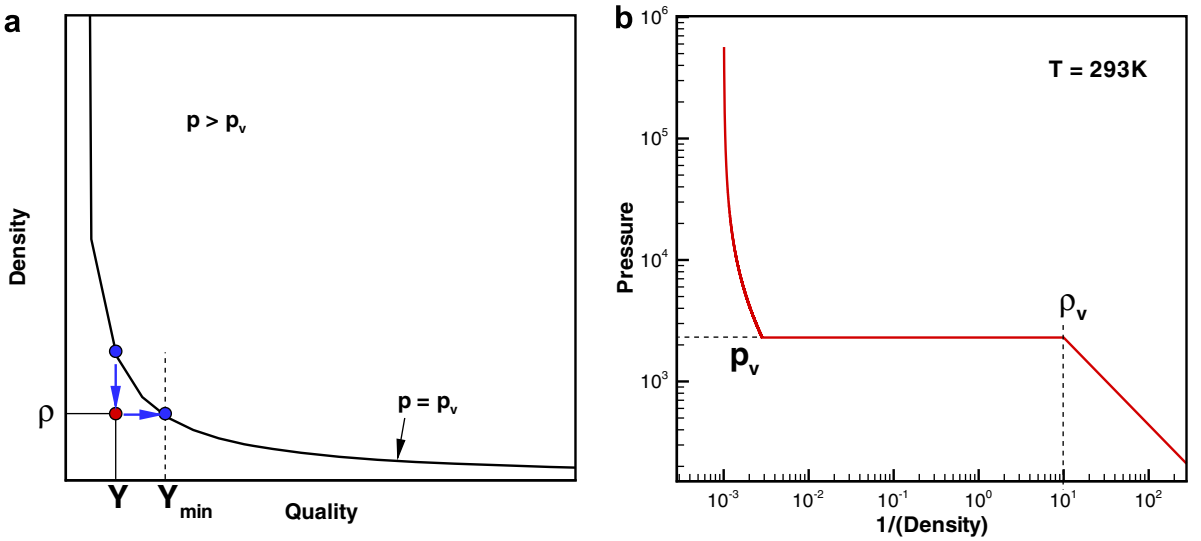

Fig. 1. (a) Schematic of phase change procedure, (b) $p-1/\rho$ diagram; Eq. (3)–(5) with progressive phase change.

$$\begin{aligned}\rho_{\mathrm{v}} &= p_{\mathrm{v}}/RT,\\ Y_{\min} &= \frac{p_{\mathrm{v}}(p_{\mathrm{v}}+p_{\mathrm{c}}) - \rho K p_{\mathrm{v}}(T+T_{\mathrm{c}})}{\rho\{R(p_{\mathrm{v}}+p_{\mathrm{c}})T - K p_{\mathrm{v}}(T+T_{\mathrm{c}})\}},\end{aligned} \tag{10}$$

where p_{v} is the vapor pressure, ρ_{v} is the density of saturated gas, and $Y_{\min}$ is the quality allowed at p_{v} and given ρ. If a local pressure is higher than the vapor pressure p_{v}, the current local quality Y is always greater than $Y_{\min}$. When the pressure is decreasing below p_{v}, the phase change occurs and physically $p = p_{\mathrm{v}}$, the local quality must be $Y_{\min}$. With this Y, pressure converges to p_{v} spontaneously and cannot drop under p_{v}. Additionally, if the local density drops under ρ_{v}, the cell can be regarded as the gas phase in whole and $Y = 1$ can be substituted. The schematic of this phase change procedure is shown in Fig. 1a and the $p \sim 1/\rho$ diagram for the present cavitation model is plotted in Fig. 1b.

3. Computational methodology

3.1. Numerical methods

The governing equations, Eq. (7) are transformed into a generalized curvilinear coordinate and written in a conservative vector form as

$$\frac{\partial Q}{\partial t} + \frac{\partial}{\partial \xi}(E - E_{\mathrm{v}}) + \frac{\partial}{\partial \eta}(F - F_{\mathrm{v}}) = 0 \tag{11}$$

where

$$Q = J\begin{pmatrix}\rho\\ \rho u\\ \rho v\\ \rho Y\end{pmatrix}, \quad E = J\begin{pmatrix}\rho U\\ \rho u U + \xi_x p\\ \rho v U + \xi_y p\\ \rho U Y\end{pmatrix}, \quad F = J\begin{pmatrix}\rho V\\ \rho u V + \eta_x p\\ \rho v V + \eta_y p\\ \rho V Y\end{pmatrix},$$

$$E_{\mathrm{v}} = J\begin{pmatrix}0\\ \xi_x\tau_{xx} + \xi_y\tau_{xy}\\ \xi_x\tau_{yx} + \xi_y\tau_{yy}\\ 0\end{pmatrix}, \quad F_v = J\begin{pmatrix}0\\ \eta_x\tau_{xx} + \eta_y\tau_{xy}\\ \eta_x\tau_{yx} + \eta_y\tau_{yy}\\ 0\end{pmatrix},$$

where J is the Jacobian of the transformation, U and V are the contra-variant velocities.

To resolve the acoustic waves in two-phase flow with minimal dispersion and dissipation errors, a high-order numerical scheme is employed in this work. Eq. (11) is spatially discretized in computational domain with a central compact finite difference scheme [24]. The sixth-order compact finite difference scheme for the first derivative is given by

$$\frac{1}{3}\frac{\partial f}{\partial \xi_{i-1}} + \frac{\partial f}{\partial \xi_i} + \frac{1}{3}\frac{\partial f}{\partial \xi_{i+1}} = \frac{14}{9}\cdot\frac{f_{i+1}-f_{i-1}}{2\Delta\xi} + \frac{1}{9}\cdot\frac{f_{i+2}-f_{i-2}}{4\Delta\xi}. \tag{12}$$

Let the compact finite difference operator with respect to ξ-direction be $C_\xi()$, the discretized form of Eq. (11) can be written as

$$Q^{n+1} = Q^n + \int_t^{t+\Delta t} \mathrm{RHS}^n \,\mathrm{d}t, \tag{13}$$

where

$$\mathrm{RHS} = -C_\xi(E - E_\mathrm{v}) - C_\eta(F - F_\mathrm{v})$$

and the superscript n denotes a time level. The metrics are also computed by the compact finite difference to retain the order of accuracy on the curvilinear coordinates [29]. The time integration in Eq. (13) is performed by a four-stage Runge–Kutta method:

$$\begin{aligned} Q^{(0)} &= Q^n \\ Q^{(k)} &= Q^n + \Delta t/(5-k)\cdot \mathrm{RHS}^{(k-1)} \quad k = 1,4 \\ Q^{n+1} &= Q^{(4)}. \end{aligned}$$

This explicit time marching is effective to resolve the small propagating compressibility effects such as acoustic waves.

For handling out-going waves, an 'Energy Transfer and Annihilating' (ETA) boundary condition [30] is applied at the far-field boundaries. The ETA boundary condition works within a buffer-zones, in which grids are rapidly stretched. Grid spacing in the buffer-zone is expressed as

$$(\Delta x)_i = x_i - x_{i-1} = C_\mathrm{ETA}\cdot(\Delta x)_{i-1}$$

where C_ETA is the stretching ratio. The value of $C_\mathrm{ETA} = 2$ and 10 grid points in the buffer-zone are suggested in Ref. [30] for most of aero-acoustic problems. In this study, smoother and wider buffer-zone ($C_\mathrm{ETA} = 1.4$ and 20 grid points) are used to resolve not only acoustic waves but also any exited vortical wakes and bubbles.

3.2. Selective spatial filtering

A numerical instability could arise even in the smooth solution because the compact scheme has no diffusion errors. Moreover, on the solution of cavitating two-phase flows, there are steep gradients including shock waves. When a compact scheme is used for such region, the solution will be suffered by severe oscillations. In order to suppress such numerical errors, a spatial filtering proposed by Gaitonde et al. [25] is applied in a selective manner.

The general formulation is given by

$$\alpha_f \tilde{f}_{i-1} + \tilde{f}_i + \alpha_f \tilde{f}_{i+1} = \sum_{n=0}^{N/2} \frac{a_n}{2}(f_{i+n} + f_{i-n}), \tag{14}$$

where N is the order of spatial filtering. The coefficients a_n for the Nth order can be found in Ref. [25]. The high-order spatial filtering (e.g. tenth-order) is only dissipative for very high wave numbers. The tenth-order filtering is ideal for smooth regions to suppress the high-frequency numerical errors with minimizing the dissipation of physical waves. For the region where steep gradients exist, a more diffusive filtering is required to suppress the oscillation errors. The second-order filtering with small value of α_f can provide enough numerical diffusion to capture the steep gradients and shock waves. In direct simulation of the cavitation noise, a

low-order filtering should be applied for numerical stability to the region where cavitation bubbles are generated and collapsed, while other regions must be dealt with the high-order filtering to resolve the acoustic wave propagation.

In this study, the spatial filtering is used in a selective manner. We apply a tenth-order filtering with $\alpha_f = 0.49$ ($F10$, hereafter) for smooth regions and a second-order filtering with $\alpha_f = 0$ ($E2$, hereafter) for regions with steep gradients. The spectral response of those spatial filtering is shown in Fig. 2. As mentioned, $F10$ filtering is dissipative only for the very high wave number ($w > 2$), while $E2$ filtering provides numerical damping through out all wave number ranges. The filtering formulation, Eq. (14) is implicit and a local order-change of filtering can be performed by locally modifying the coefficients of the matrix. In order to estimate a smoothness of local solution, the following criterion is used:

$$\begin{aligned} &\Delta_2 = |f_{i+1} - 2f_i + f_{i-1}| \\ &\begin{cases} \Delta_2 \geqslant C_s(f_{\max} - f_{\min}) & E2 \text{ filtering} \\ \Delta_2 < C_s(f_{\max} - f_{\min}) & F10 \text{ filtering} \end{cases}, \end{aligned} \tag{15}$$

where $f_{\max}$ and $f_{\min}$ are the global maximum and minimum values and C_s is an arbitrary constant. In our study, we found that a value of $C_s = 0.1$–0.2 works well. Actually, C_s controls the oscillation errors and resolutions of the high-frequency 'physical' waves. With small C_s, there are small oscillation errors near the steep gradients but some high frequency waves are diffused. For large C_s, the case is vice versa. There are many other ways to estimate the solution smoothness but this simple procedure is sufficient for now. A study for finding a more optimized smoothness estimator will be pursued in the future study.

The resulting formulation of selective spatial filtering can be written as

$$(1-\beta)\alpha_f \tilde{f}_{i-1} + \tilde{f}_i + (1-\beta)\alpha_f \tilde{f}_{i+1} = \beta \frac{f_{i+1} + 2f_i + f_{i-1}}{4} + (1-\beta)\sum_{n=0}^{5} \frac{a_n}{2}(f_{i+n} + f_{i-n}), \tag{16}$$

where

$$a_0 = \frac{193 + 126\alpha_f}{256}, \quad a_1 = \frac{105 + 302\alpha_f}{256}, \quad a_2 = \frac{-15 + 30\alpha_f}{64},$$
$$a_3 = \frac{45 - 90\alpha_f}{512}, \quad a_4 = \frac{-5 + 10\alpha_f}{256}, \quad a_5 = \frac{1 - 2\alpha_f}{512},$$

$\alpha_f = 0.49$ and β is a parameter determined by Eq. (15), i.e. $\beta = \{1 + \mathrm{sgn}(\Delta_2 - C_s(f_{\max} - f_{\min}))\}/2$.

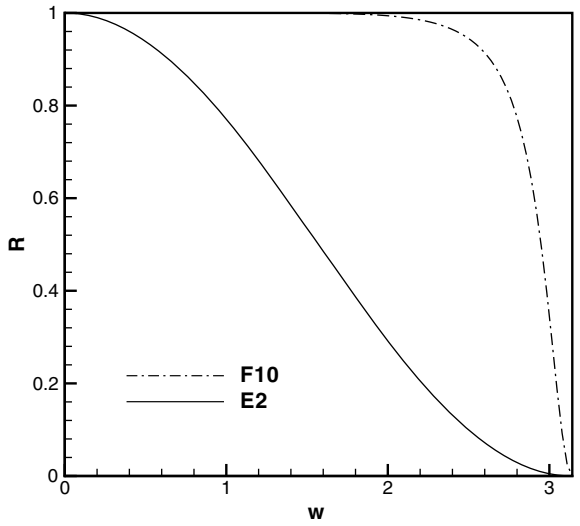

Fig. 2. Spectral response of spatial filtering, where $R = \tilde{f}/f$ and $w = k\Delta x$ is a modified grid wave number.

4. Benchmark problems

4.1. 1D wave equation

A purpose of the compact scheme with selective filtering is to resolve not only the steep gradients with minimal oscillation errors but also the smooth high frequency waves without loss of peak. To test the aforementioned numerical scheme, 1D wave equation

$$\frac{\partial u}{\partial t}+\frac{\partial u}{\partial x}=0$$

is considered with an initial condition, which includes a steep square wave and a smooth high-frequency Gaussian wave. The domain is set to $0 \leqslant x \leqslant 3$ and the domain edges are periodically connected. The initial condition is given by

$$u(0,x)=\begin{cases}1.0 & \text{for } 0.8 \leqslant x \leqslant 1.2\\ \exp\left(-\left(\frac{x-2}{0.05}\right)^2\right) & \text{otherwise.}\end{cases}$$

The 1D wave equation is solved by the sixth-order compact scheme with selective filtering (C6SF), $r=3$ WENO scheme [22] (WENO3), and upwind TVD scheme [31] (TVD) for comparison. The formal order of accuracy of each scheme is estimated as hybrid second-order and sixth-order for C6SF, varied from third-order to fifth-order for WENO3, and second-order for TVD scheme. The parameters used for the computations are $\Delta x=0.01$, CFL $=0.5$, and $C_s=0.1$ (for the selective filtering). The computed solutions at $t=6$ are shown in Fig. 3 with the exact solution. For the square wave, there are small overshoots and undershoots found in the C6SF solution but this error is unavoidable for this central scheme. With the $E2$ filtering, the error is relatively small and also bounded. The WENO3 and TVD schemes do not produce oscillation errors because they are the upwind schemes. On the other hand, a noticeable peak loss is observed in the WENO3 solution and the TVD solution is too dissipative in this case to resolve the high-frequency wave.

The effect of parameter C_s in selective spatial filtering and its grid dependancy are also investigated in Fig. 4. As mentioned above, a large value of $C_s(=0.2)$ allows more oscillation errors. With small value of $C_s(=0.05)$, a square wave is well captured smoothly but the peak loss is observed for this high frequency wave, like a trade-off. It is found that the value of 0.1 is most well balanced. There is no peak loss in the high frequency wave and the oscillation errors near the square wave are also quite small. The grid dependancy of

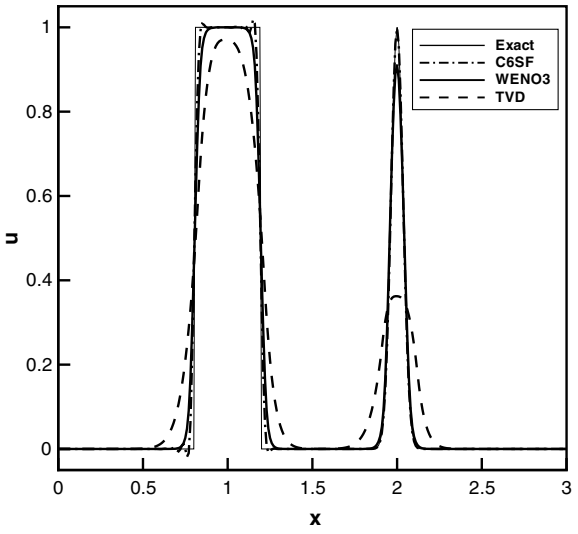

Fig. 3. 1D square wave and Gaussian pulse convection; comparison of numerical schemes.

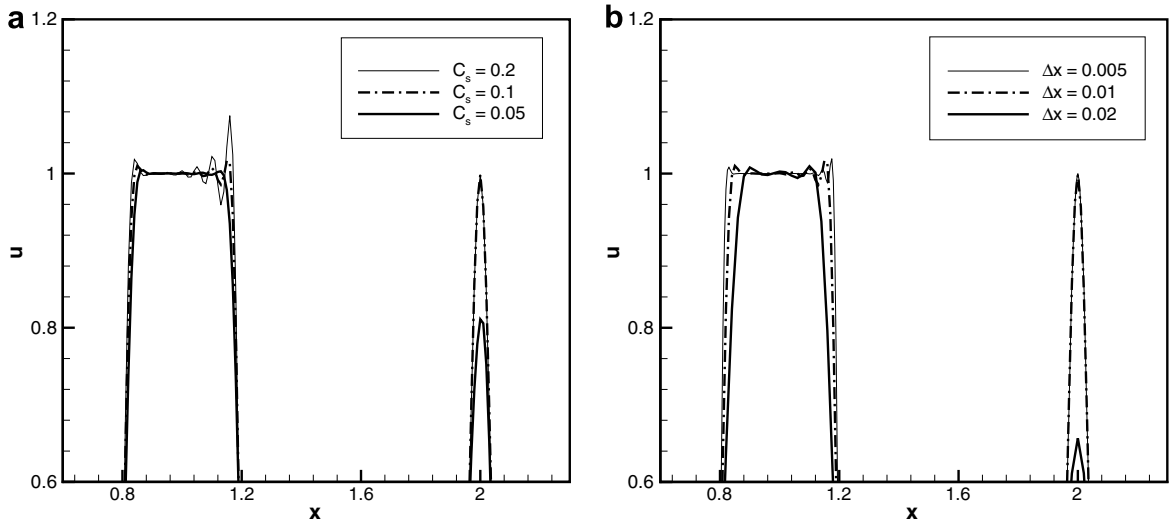

Fig. 4. 1D square wave and Gaussian pulse convection; (a) effect of parameter C_s, (b) effect of grid size for $C_s = 0.1$.

selective filtering is studied for $C_s = 0.1$ on three different grids. As one can see in Fig. 4b, oscillations near the discontinuity are bounded for all three cases. Note that $\Delta x = 0.02$ is too coarse grid size for the Gaussian wave. From these results it is shown that the preferred value of $C_s = 0.1$ are almost independent of grid size for acceptable range. Therefore, $C_s = 0.1$ is used for all other computations in this study. Though the C6SF scheme is not perfect yet, the solution is surely acceptable, considering its easiness in practical usages.

4.2. Acoustic saturation in a bubbly cavitating flow

In this section, we test our homogenous equilibrium model and C6SF scheme for a simple cavitating flow with wall oscillations. In bubbly flows, acoustic waves generated by wall oscillations are steepened due to the non-linear effects and the acoustic saturation is followed, i.e. the radiated acoustic energy is not increased as the amplitude of wall oscillations is increased. This problem was studied by Colonius et al. [8], using the Rayleigh–Plesset equation. We consider a semi-infinite region bounded by a flat moving wall. The wall boundary condition is that a fluid velocity normal to the wall is equal to the wall velocity. A sinusoidal motion of the wall given by

$$u_w = A\sin(2\pi(t/T)),$$

where A is the amplitude and T is the period of wall oscillations. For bubbly flows, an initial void fraction is set to $\alpha = 0.01$ and a one-dimensional form of Eq. (7) is solved with the equation of state, Eq. (5). A grid spacing is 0.01λ, where λ is the acoustic wave length. A selective filtering is applied with $C_s = 0.1$ and the smoothness is estimated only by the pressure.

For the small amplitude of wall vibration velocity, the non-linear effects are absent and wall vibrations generate propagating disturbances. For large amplitude, compression waves are steepened into shock waves that take a periodic train of N waves. The waves are then dissipated when compression waves are steepened into shocks further, which is similar to the acoustic saturation phenomenon mentioned by Colonius et al. [8].

On the acoustic saturation, the maximum pressure along the distance from the wall can be obtained analytically from a weak shock analysis [32]. The maximum pressure is given by

$$p_{\max} = \begin{cases} p_A & \text{if } x < \frac{\pi\rho_0 c_0^3}{2\beta_0 p_A \omega} \\ \dfrac{\pi p_A}{1 + p_A\left(\frac{x\beta_0\omega}{\rho_0 c_0^3}\right)} & \text{if } x > \frac{3\pi\rho_0 c_0^3}{\beta_0 p_A \omega} \end{cases}, \tag{17}$$

where p_A is the amplitude of pressure oscillations at the wall, ρ_0 and c_0 are the ambient density and speed of sound, ω is the frequency of oscillations, and β_0 is a thermodynamic quantity given by

$$\beta_0 = 1 + \rho_0 c_0 \left(\frac{\partial c}{\partial p}\right)_0.$$

The quantity β_0 is a measure of non-linear steepening of the waves. The larger values of β_0 imply that shocks are formed with smaller amplitude of vibrations. For ideal gas, $\beta_0 = (\gamma + 1)/2$. Colonius et al. calculated β_0 for bubbly fluids from the equations of bubble dynamics. In this study, the equation of state for the homogeneous equilibrium model is directly used to find β_0. To apply Eq. (17) to a two-phase flow, Eq. (6) is re-written as

$$c^2 = \frac{p(p + p_c)}{(p + \alpha p_c)\rho} \simeq \frac{p}{\alpha\rho}. \tag{18}$$

This can be differentiated with respect p to obtain β_0. For small α, it becomes

$$\beta_0 \simeq \frac{1}{\alpha}. \tag{19}$$

This value is the same as that obtained by Colonius et al. from the bubble dynamics but for an 'isothermal' process (polytropic index $k = 1$). It means that the equation of state for the homogenous equilibrium model well depicts the characteristics of two phase flow as bubble dynamics does.

Eq. (17) is compared in Fig. 5 with the computed pressure as a function of distance from the wall, for several amplitudes of wall vibrations. The pressure is apparently well predicted. As predicted by Eq. (17), acoustic

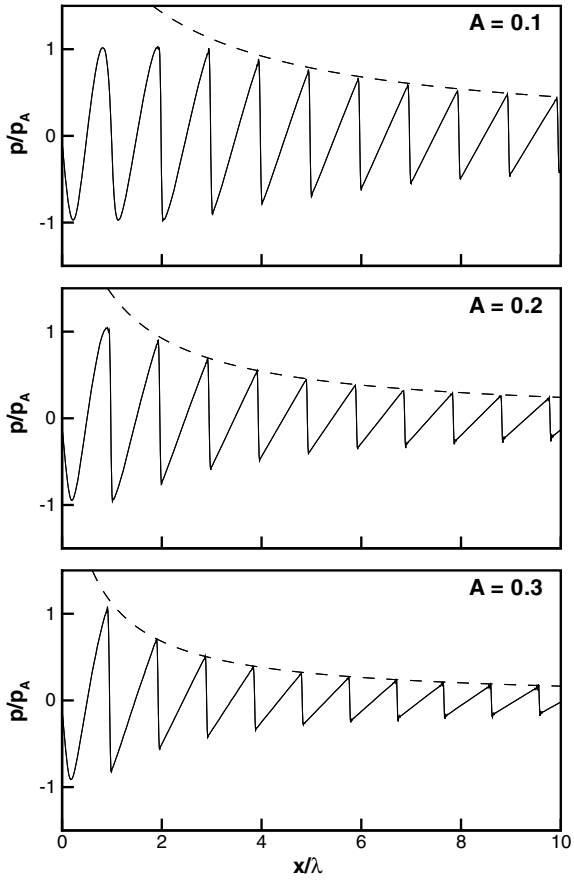

Fig. 5. Spatial evolution of pressure (normalized) in a bubbly flow; dashed lines are the maximum pressure predicted by Eq. (17).

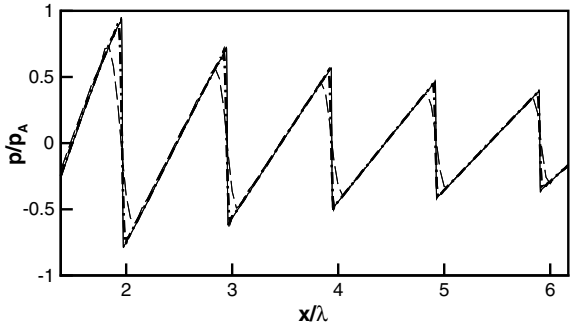

Fig. 6. Grid convergence study; solid line: $\Delta x = 0.0025\lambda$, dash-dotted: $\Delta x = 0.01\lambda$, dashed: $\Delta x = 0.04\lambda$.

saturation occurs close to the wall as the amplitude is increased. At the highest amplitude, shocking of the wave is immediate. These results are very much the same as those of Colonius et al. [8]. Through this benchmark problem, it is shown that the saturation phenomena in a bubbly cavitating flow are well predicted by the homogeneous equilibrium model and the present C6SF scheme.

The grid convergence study is also performed for this non-linear problem with more significant change of grid size (by a factor by four). For $A = 0.2$ case, additional computations are made with four times finer and coarser grids. Fig. 6 shows that the computed result with four times finer grid is almost identical to that for the normal grid and only slightly smeared profile is observed for the four times coarser grid. It is clear that the grid convergence of C6SF scheme has been achieved with $C_s = 0.1$.

5. Results and discussion

5.1. Cavitating flow over a 2D circular cylinder

In this study, a two-phase, cavitating flow past a 2D circular cylinder is directly simulated with the density-based homogeneous equilibrium model and C6SF numerical scheme. A bubbly flow over the cylinder with ambient void fraction of $\alpha_0 = 0.01$ is assumed for an isothermal state at $T_0 = 293$ K. The inlet flow speed is $u_0 = 10$ m/s and the Reynolds number of the flow is limited to $Re_D = \rho_0 u_0 D/\mu_0 = 200$, where D is the diameter of a cylinder, to exclude any three-dimensional, turbulent nature of the flow. The cavitation number σ is defined by

$$\sigma = \frac{p_0 - p_v}{0.5\rho_0 u_0^2}, \tag{20}$$

where p_v represents a vapor pressure. To adjust the cavitation number, ambient pressure is modified accordingly and three test flow conditions, $\sigma = 2, 1$, and 0.7 are considered in the present study.

For direct computation of cavitating flow and noise, a computational domain for o-type grid is chosen with outer boundary at $r = 100D$ to include several acoustic wavelengths. The grid points of 201×301 are distributed in the circumferential and radial directions, respectively, with minimal normal grid spacing of $0.01D$ at the wall. A selective filtering is applied with $C_s = 0.1$ and the smoothness is estimated with the pressure gradient only. For this cavitating flow, the grid cells with phase change are marked and filtered by $E2$ filtering because the flow Mach number in such region often exceeds the sonic speed.

For each cavitation number, the instantaneous void fraction and vorticity fields around the cylinder are presented in Fig. 7. For large cavitation number ($\sigma = 2$), cavitation bubbles are not generated because the static pressure do not drop below the vapor pressure at $Re_D = 200$. Hence, the flow patterns, drag and lift coefficients, and Strouhal number of the Karman vortex shedding frequency ($St = fu_0/D = 0.19$) are very similar to those for the single phase flow (e.g. $St = 0.196$ for a two-dimensional cylinder [33]). The time-averaged drag coefficient, $\overline{C_D} = 1.08$ is slightly smaller than the value for single phase flow, $\overline{C_D} = 1.33$ [34,35]. For small cavitation numbers, however, the static pressure drops below the vapor pressure at the cylinder surface and also with the vortex shedding. Therefore, vortex cavitation is generated via phase-change. At $\sigma = 1$, cavitation

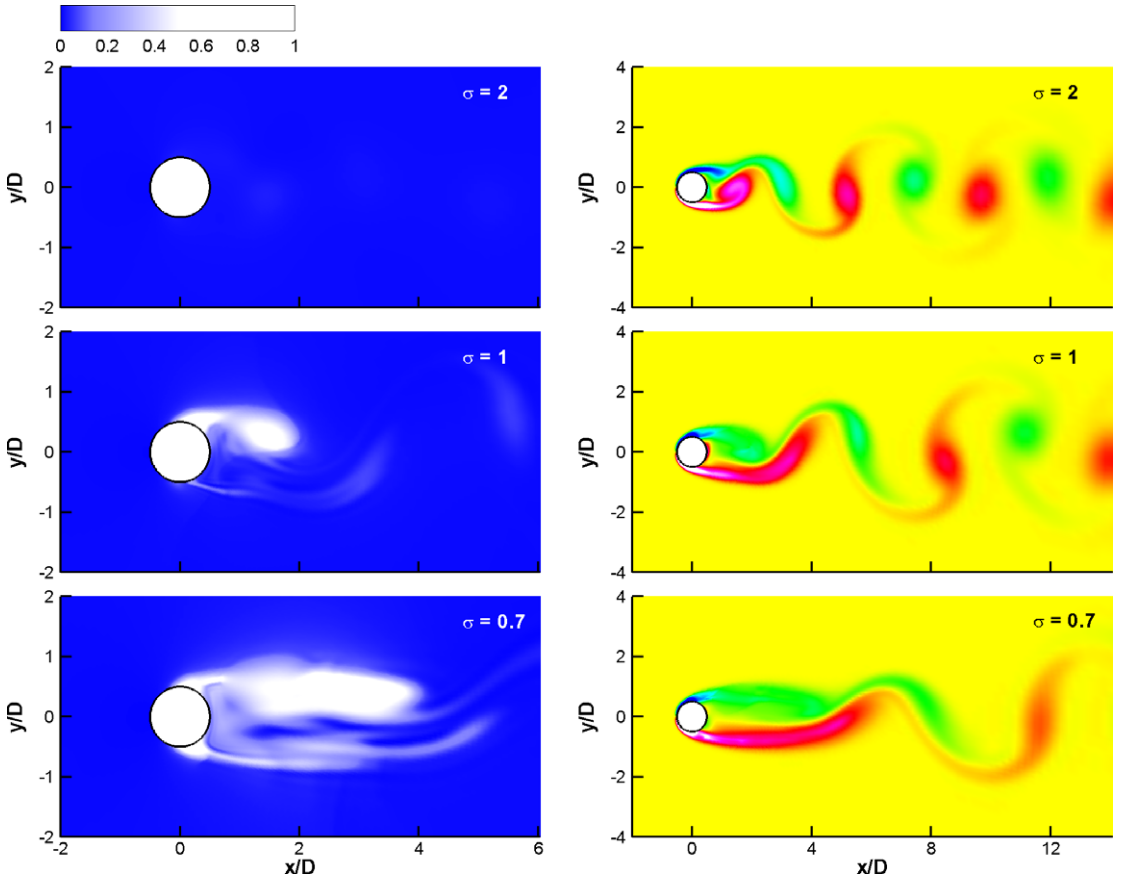

Fig. 7. Two-phase flow over a 2D cylinder for cavitation numbers, $\sigma = 2, 1$, and 0.7; left: instantaneous void fraction, right: vorticity at a same instant.

bubbles are periodically generated by fluctuations of pressure due to the vortex shedding, though a mean pressure itself does not reach the vapor pressure p_v. At $\sigma = 0.7$, the mean pressure on the cylinder surface drops below p_v and cavitation bubbles are widely distributed with large values of void fraction but steady or fixed cavity is not observed in the cylinder wake. Both cavitation number $\sigma = 1$ and 0.7, therefore, fall within the case of cyclic cavity development in wake [36]. As one can see in Fig. 7, the cavitation bubble is detached from the cylinder surface with vortex shedding and therefore unsteady distribution of the void fraction marginally coincides with the vorticity field. The bubble cloud detached from the cylinder surface will finally collapse during exposure to the surrounding higher pressure fluids. The shedding and collapse of the cavitation bubble along with the vortex shedding were investigated experimentally by Saito and Sato [37].

To examine the unsteady flow characteristics, time histories of drag and lift coefficients are plotted in Fig. 8. In the present computation, shock waves or impacts generated by the collapse of cavitation bubbles can be clearly identified with $\sigma = 1$. For $\sigma = 1$ and 0.7 (cavitating flows), drag and lift coefficient profiles look quite different from that of $\sigma = 2$ (non-cavitating flow). Especially at $\sigma = 1$, drag and lift forces are severely affected by the shock waves and so the time evolution of the lift coefficient clearly exhibits a pattern of N-waves. As cavitation number decreases from 1 to 0.7, generation and collapse of the cavitation bubble become less periodic due to the increased volume of cavitation bubbles. It is also interesting to note that the formation of cavitation bubbles on the cylinder surface changes the vortex shedding structure as well as the frequency. The larger cavity delays the vortex shedding and makes the vortex shedding period longer. The Strouhal number for the vortex shedding becomes $St = 0.16$ for $\sigma = 1$ and $St \simeq 0.13$ for $\sigma = 0.7$, as compared to the non-cavitating case ($St = 0.19$ for $\sigma = 2$). In the present computation, a very low frequency phenomenon at $St \sim 0.03$ is also observed in Fig. 8 at $\sigma = 0.7$. The decrease of shedding frequency with decreasing cavitation number is

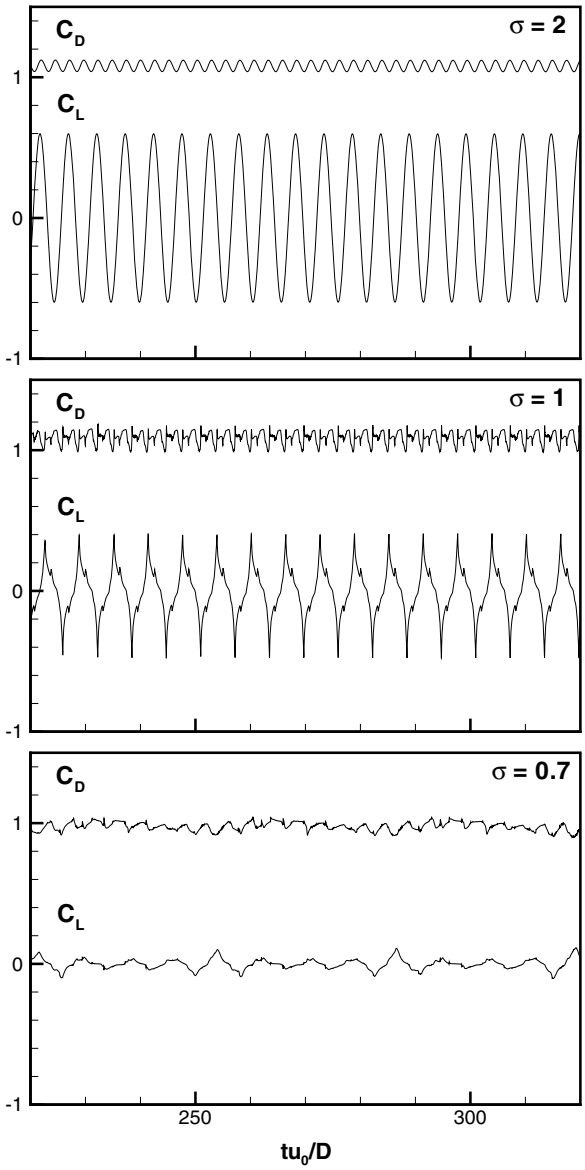

Fig. 8. Drag and lift coefficients for cavitation numbers, $\sigma = 2, 1$, and 0.7.

also investigated and reported by previous researchers [38,39] for a circular cylinder with cyclic cavity development in wake. At further lower cavitation number, however, it is reported that the shedding frequency increased with the development of fixed, steady cavity in wake [36,38]. While Ausoni et al. recently observed that the frequency of Karman vortex shedding increased with decreasing cavitation number in the early stage of cavitation inception for a blunt-trailing edge hydrofoil [40]. The reason of this frequency increasing is also supposed to be the presence of early developed fixed cavity due to the geometric shape.

Before proceeding to further study, it is useful to investigate the assessment of grid resolution. The case of $\sigma = 1$ is computed on the grid of finer resolution, 401×601 and the results are compared in Fig. 9 with the normal grid case (201×301). Fig. 9a shows time history of drag and lift coefficients for fine and normal grids. There is no significant difference between two results. In Fig. 9b, instantaneous pressure fields are also compared. The overall structure of pressure field, including cavity region and shock waves are resolved almost identically with the fine and normal grids, except that the detailed structures are resolved more sharply with

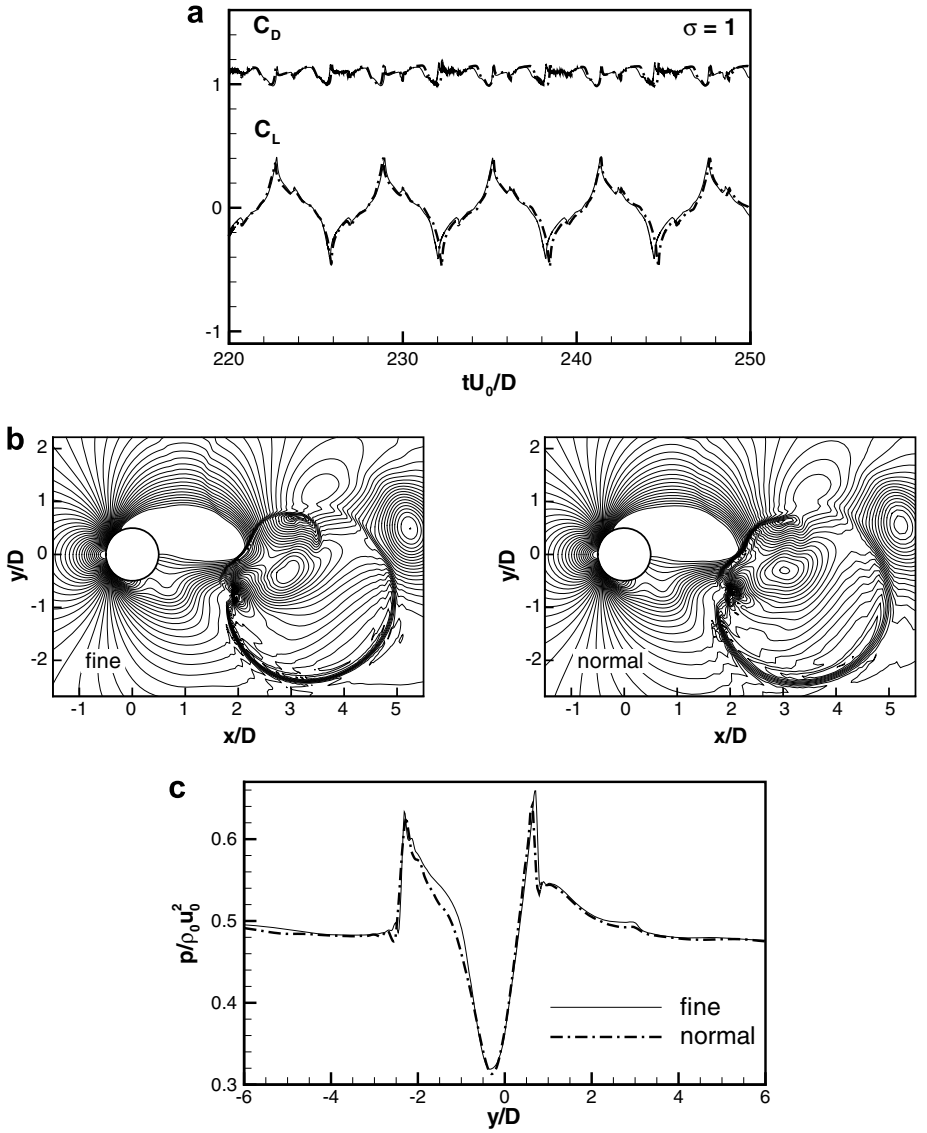

Fig. 9. Grid-resolution assessment, (a) drag and lift coefficients; solid: fine (401 × 601), dash-dotted: normal (201 × 301), (b) instantaneous pressure field, (c) pressure profile along $x/D = 3$ line.

the fine grid. For the quantitative comparison, the pressure profile is extracted along $x/D = 3$ line which crosses the pressure discontinuities, and it is presented in Fig. 9c for both fine and normal grids. As one can see in the figure, discontinuous pressure profiles resolved on both grids are in close agreement.

5.2. Cavitating flow noise

A rapid volume change of cavity or collapse of cavitation bubbles emits shock waves. This pressure pulse is generally known as a main source of the cavitation noise. In the present direct simulation, the generation of pressure pulse and its propagation to the far-field are fully resolved with C6SF numerical scheme. The fluctuating pressure fields ($p' = \bar{p} - p$) generated by the two-phase flow over the 2D cylinder are presented in Fig. 10. A typical cylinder dipole tone is observed in Fig. 10a for $\sigma = 2$. This dipole tone is caused by the pressure fluctuations at either side of the cylinder top and bottom due to the von Karman vortex shedding and looks very much the same as in aero-acoustics of the laminar flow past a circular cylinder. For smaller cav-

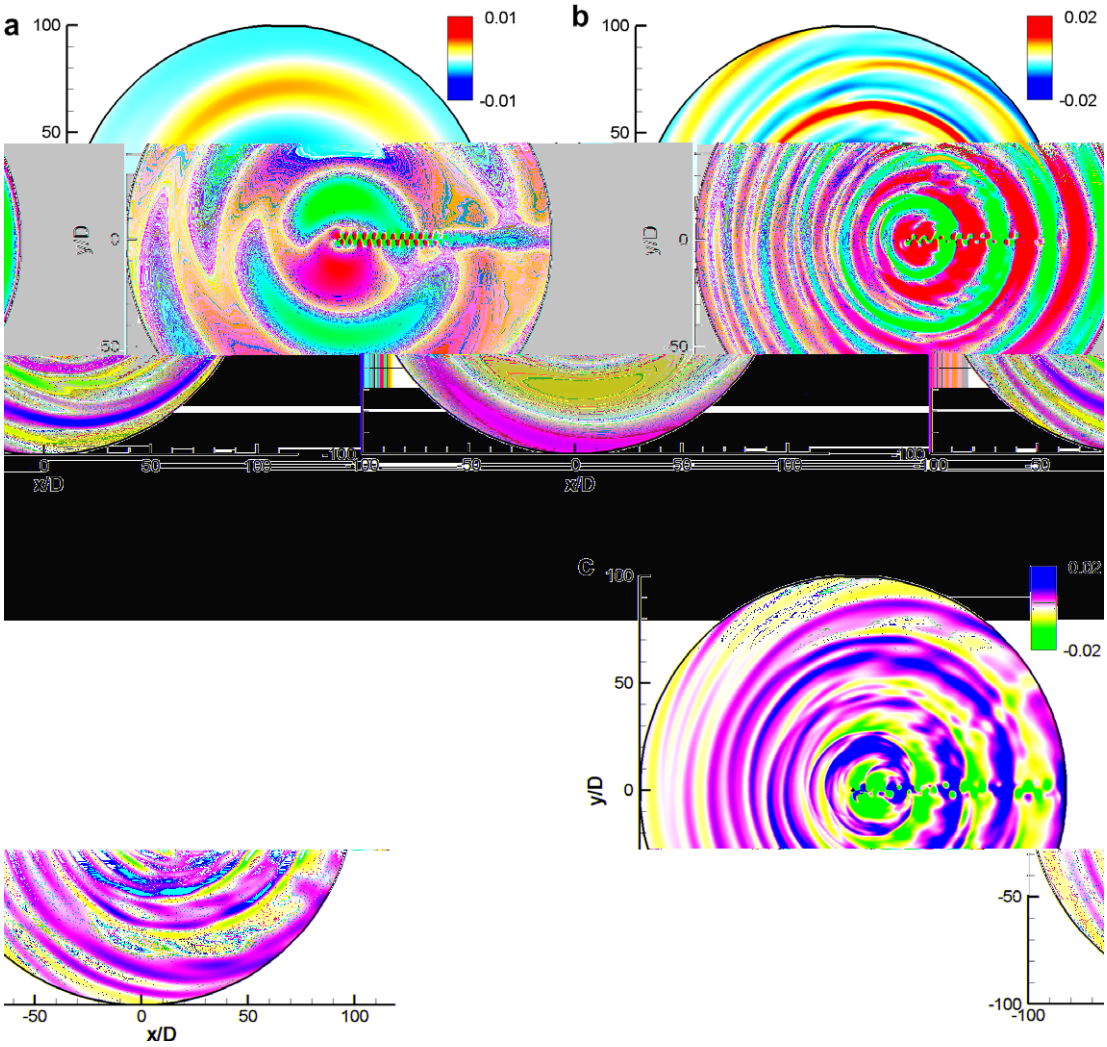

Fig. 10. Pressure fluctuation fields: (a) $\sigma = 2$, (b) $\sigma = 1$, and (c) $\sigma = 0.7$; normalized by $\rho_0 u_0^2$.

itation numbers ($\sigma = 1$ and 0.7), however, pressure fluctuation fields look quite different. The monopole-like pressure waves observed in Fig. 10b and c are the propagating shock waves generated by the collapse of cavitation bubbles. These shock waves are generated at the point, where the bubble is broken-off and collapsed. The high-frequency waves clearly identified in Fig. 10b may also be generated via interactions of the shock waves with the cavity cloud in the vortex train downstream of the wake.

Fig. 11 shows the time history of pressure fluctuations monitored at $r = 70D$ directly above the cylinder for each case. As expected, a sinusoidal acoustic wave is observed for $\sigma = 2$ (non-cavitating flow), while cavitating flows ($\sigma = 1$ and 0.7) generate shock waves, which are typical for the collapse of cavitation bubbles [6,7]. At $\sigma = 1$, two peaks are observed for one period, due to the break-off and collapse of the bubbles by alternating vortex shedding. The signal of $\sigma = 0.7$ is much less periodic because a low frequency wave is imposed. For cavitating flows, shock waves generated by the collapse of cavitation bubble are regarded as the noise source, which is stronger than the pressure fluctuations by Karman vortex shedding.

The power spectral densities (PSD) of the pressure fluctuations monitored at $r = 70D$ for three cases are presented in Fig. 12. At $\sigma = 2$, noise is purely from the surface dipole and has a spectral peak at the vortex shedding frequency ($St = 0.19$). For $\sigma = 1$, however, the dominant noise is the monopole-like shock waves generated by breakdown and collapse of the alternating cavitation bubble and the peak is observed at the

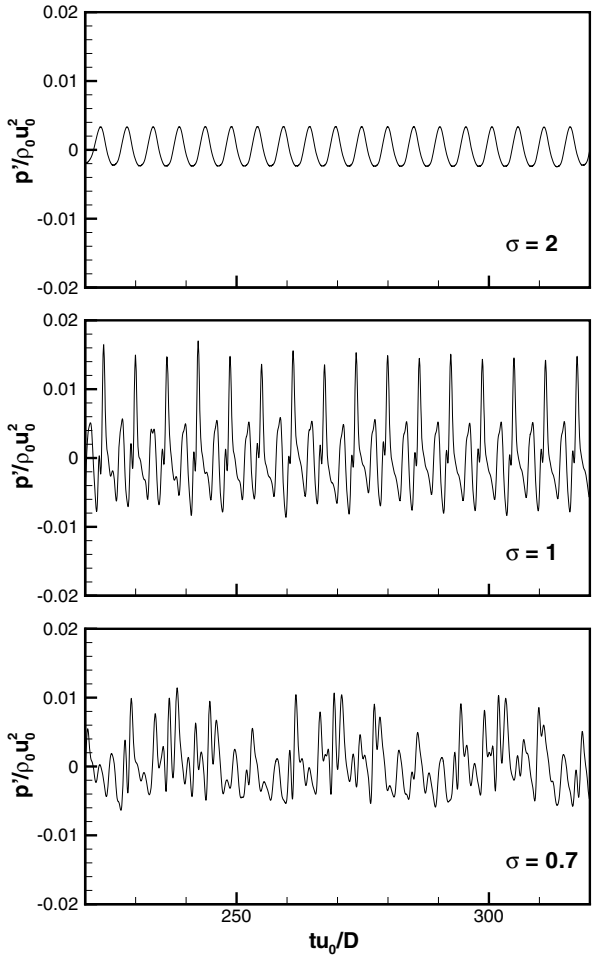

Fig. 11. Pressure fluctuation monitored at $r = 70D$; non-dimensionalized by $\rho_0 u_0^2$.

double of the vortex shedding frequency ($St = 0.32$). As mentioned, the Strouhal frequency decreases, as the cavitation number decreases (e.g. $St = 0.19, 0.16$ and 0.13 for $\sigma = 2, 1$, and 0.7) because the vortex shedding is delayed due to the formation of cavitation bubble. For $\sigma = 0.7$, the peaks are made not only by the alternate collapse of the cavitation bubble (at $St = 0.26$) but also by the low frequency behavior of the elongated vortex cavity (at $St \sim 0.03$). The breakdown and collapse of the cavitation bubble with vortex shedding are also affected by this low frequency behavior, which makes the noise spectrum broadened. It is also found that the noise level for the cavitating flow case is much higher than that for the non-cavitating case.

5.3. Shock wave generation by collapsing clouds

A transient process of shock wave generation during the collapse of cavitation bubble cloud is closely examined to identify its coherences with the radiated cavitation noise. A time evolution of the pressure fluctuations at $\sigma = 1$ is presented in Fig. 13 for a half period along with the void fraction. In early stage, the sheet cavitation at the upper cylinder surface is breaking-off by the Karman vortex shedding and cloud cavitations are formed. The front part of cavity cloud remains on the cylinder surface, while the rear part(sub-cloud of forth) convects downstream with the shed vortex. As soon as the pressure is recovered at the upper cylinder surface, the front bubble cloud collapses (indicated in figure as C1) and emits a shock wave (S1). The sub-

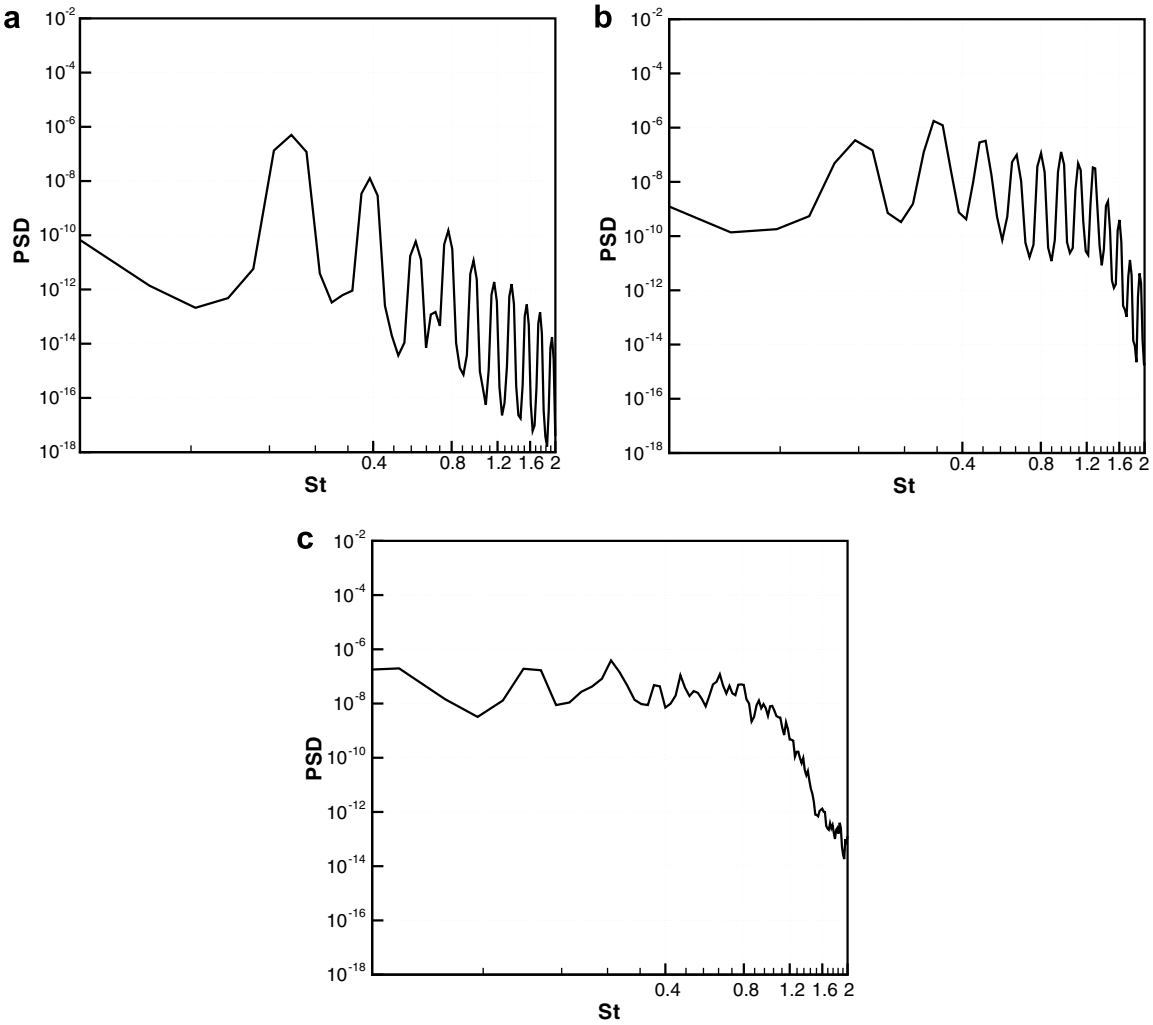

Fig. 12. Power spectral densities of pressure fluctuations at $r = 70D$, (a) $\sigma = 2$, (b) $\sigma = 1$, (c) $\sigma = 0.7$; pressure is non-dimensionalized by $\rho_0 u_0^2$ and $St = fu_0/D$.

cloud exposed to the surrounding high-pressure fluids is then shrunk by an interaction with the emitted shock wave (S1) and collapsed afterwards in the wake (C2). As a result, a stronger shock wave (S2) is generated in the wake and propagates as a monopole sound pulse. A slight rebounding of the collapsed cloud is also observed in the last snapshot. The same collapse and shock wave generation processes are repeated at the opposite side during the rest of the period. The cavitation noise generation mechanism for $\sigma = 0.7$ is basically the same. The elongated bubble cloud is collapsed and emits a shock wave at the upper and lower sides alternatively at the vortex shedding frequency, while the formation and collapse of the sub-cloud with vortex shedding is now affected by the low frequency behavior of the main vortex cavity (at $St \sim 0.03$), which is caused by the instability of the large cavitation bubble.

The computed results are found consistent with the previous work by Reisman et al. [2], who experimentally investigated the cloud cavitation noise generated by the collapse of cloud for an oscillating hydrofoil. In their experiment, the cloud cavitation is formed via breakdown of sheet cavitation over the hydrofoil with oscillation of angle of attack. They pointed out that the collapse of separated 'sub-cloud' is the main source of strong noise generation and erosion damages because the sub-cloud is sometimes very coherent and may persist well after the remains of the sheet cavity have dispersed. In the present direct simulation, the sheet cavitation over the cylinder surface is broken-off with the Karman vortex

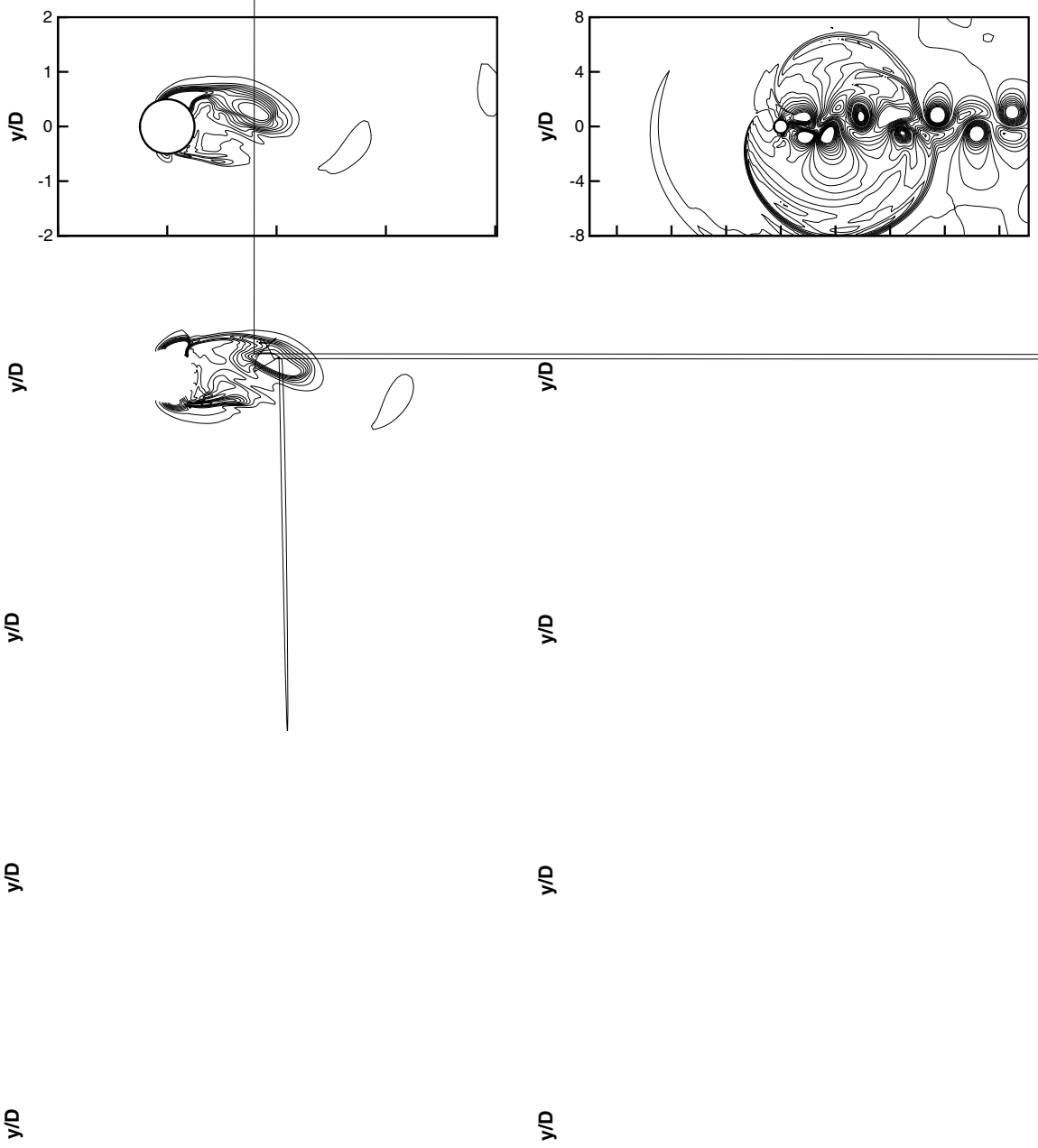

shedding and the detached vortex cavity turns into a cavity cloud. Finally, a strong pressure pulse is generated by the collapse of sub-cloud. From this comparison, it seems clear that a strong cavitation noise is originated from the shock wave generated by the collapse of sub-cloud – a possible mechanism for the cloud cavitation noise.

5.4. Comparison with theory

In this section, an acoustic analogy is derived for the cavitation noise and the predicted far-field noise is compared with that of direct simulation. The source of cavitation noise is the pressure pulse (or shock wave) generated by the collapse of cavitation bubble. Theoretically, a monopole noise generated by the collapse of single spherical bubble can be estimated by the following formulation [41,42];

$$p' = \frac{\rho_l}{4\pi r}\frac{\mathrm{d}^2 V_\mathrm{B}}{\mathrm{d}t^2}, \tag{21}$$

where r is the distance between the bubble and the measurement and V_B is the bubble volume. As one can see in Eq. (21), the volume acceleration is the source of monopole noise.

For clouds of cavitation bubble in arbitrary shape (not spherical or cylindrical), the volume of the vapor bubble can be calculated by integrating the void fraction;

$$V_\mathrm{B} = \int_V \alpha \,\mathrm{d}V, \tag{22}$$

and an acoustic analogy for the cavitating flow noise can be written as

$$4\pi p' = \underbrace{\int_V \left[\frac{\rho_0}{r}\frac{\mathrm{d}^2\alpha}{\mathrm{d}t^2}\right]_\mathrm{ret} \mathrm{d}V}_{\mathrm{I}} + \underbrace{\int_S \left[\frac{\cos\theta}{c_0 r}\frac{\mathrm{d}p}{\mathrm{d}t}\right]_\mathrm{ret} \mathrm{d}S}_{\mathrm{II}} \tag{23}$$

where 'ret' denotes a value estimated at retarded time, $t - r/c_0$. Term I is the modeled source for the monopole noise, which would be generated by the collapse of bubble clouds, and the surface integral, term II is the dipole source exerted by the pressure fluctuations over the body surface. A quadruple noise by turbulence fluctuations is excluded in the present study. The modeled cavitation monopole source (term I) is based on a classical theory, Eqs. (21) and (23) converges to Eq. (21) for a single bubble. In the frequency domain, Eq. (23) is written as

$$4\pi\hat{p}' = \int_V \frac{\mathrm{e}^{\mathrm{i}kr}}{r}\rho_0\omega^2\hat{\alpha}\,\mathrm{d}V + \int_S \frac{\mathrm{e}h^{\mathrm{i}kr}}{r}\mathrm{i}k\cos\theta\hat{p}\,\mathrm{d}S, \tag{24}$$

and its two-dimensional form is expressed as

$$4i\hat{p}' = \int_V \rho_0\omega^2\hat{\alpha}H_0^{(2)}(kr)\,\mathrm{d}V + \int_S \cos\theta\cdot k\hat{p}H_1^{(2)}(kr)\,\mathrm{d}S, \tag{25}$$

where H is the Hankel function and $k = \omega/c_0$.

Eq. (25) is now used to predict the cavitating flow noise from a 2D circular cylinder. The time-dependent surface pressure fluctuations and void fraction fields are obtained from the computational results presented in Section 5.1. The power spectral densities of the acoustic pressure predicted by Eq. (25) are now compared with that of direct computation for $\sigma = 1$ and 0.7. As one can see in Fig. 14, they are in excellent agreement, showing that the overall shape of the spectrum is very much the same. For $\sigma = 1$, the first and second peak levels are very well met. A little discrepancy observed in $\sigma = 0.7$ case may be caused by the near-field, non-linear effects due to the larger void fraction. The high-frequency cut-offs in direct simulation are just caused by the lack of grid resolution at the far-field. From this comparison, it is convinced that the present cavitation model and numerical methods consistently resolve the physics of cavitation noise.

For the present cavitating flow over the blunt body, the radiated noise is composed of monopole by cavitation bubble collapsing and surface dipole as discussed. With the aid of above acoustic analogy, the radiated noise can be evaluated by quantifying the importance of each term. Fig. 15 shows the monopole and dipole parts separately for $\sigma = 1$ and 0.7. As investigated, a dipole peak is at the vortex shedding frequency, while the monopole peak is twice the vortex shedding frequency. In overall, the bubble collapsing yields the noise level higher than the surface dipole. For transient cavitating flow ($\sigma = 1$), bubble collapsing occurs

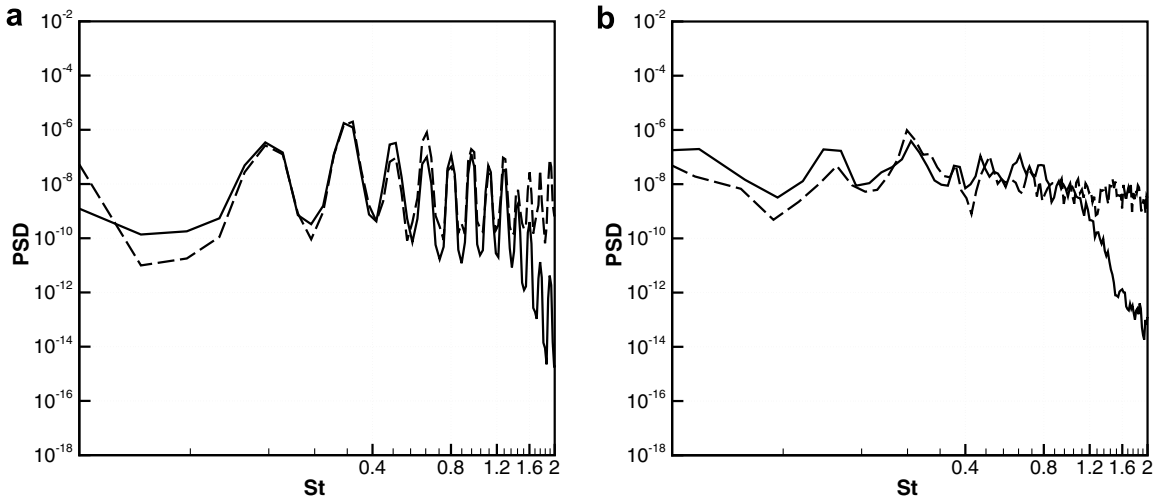

Fig. 14. Power spectral densities of normalized acoustic pressure fluctuations at $r = 70D$, (a) $\sigma = 1$, (b) ($\sigma = 0.7$); –: direct computation, - -: Eq. (25), pressure is non-dimensionalized by $\rho_0 u_0^2$ and $St = fu_0/D$.

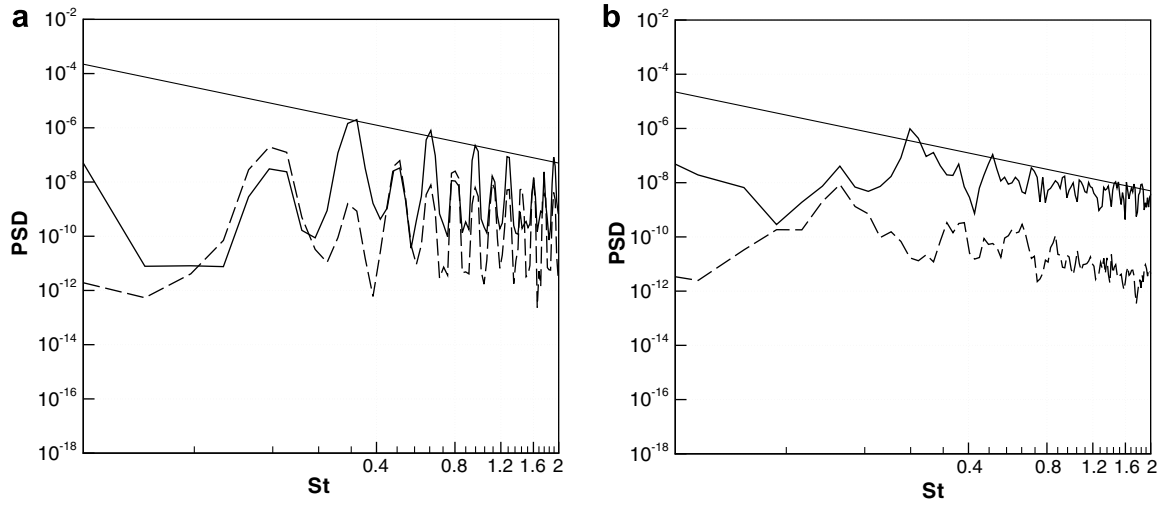

Fig. 15. Power spectral densities of normalized acoustic pressure fluctuations at $r = 70D$, (a) $\sigma = 1$, (b) $\sigma = 0.7$; –: monopole noise by bubble collapsing, - -: surface dipole noise, slope: f^{-2}.

near the body and surface pressure fluctuations are affected by the collapsing. In this case, the surface dipole noise is amplified by the impact force exerted by the bubble collapsing and the noise can be considered as an 'impact dipole' noise. For a certain cavitating flow, this impact dipole noise caused by the bubble collapsing near the body could be the dominant noise source because a strong correlation is observed between the body force (lift force) and the radiated noise [3]. At $\sigma = 0.7$, the vortex shedding and bubble collapsing occur farther downstream as shown in Fig. 7, and the surface dipole level is much lower than the cavitation monopole. In such case, the bubble collapsing can be considered the dominant noise source. In addition, it is known that the high-frequency part of the cavitation noise decays as f^{-n}, where $n = 0.5$–2 [41–43]. In Fig. 15, one can clearly notice that the predicted cavitation monopole noise closely follows the f^{-2} decaying, as predicted by the model of Fitzpatrik and Strasberg [4] with the Rayleigh–Plesset equation. The spectrum of noise radiated by the single bubble cloud predicted by Wang and Brennen [6,7] also exhibits a f^{-2} decaying.

6. Conclusions

A direct numerical simulation procedure for the cavitating flow noise is presented. As demonstrated in two benchmark problems, the present computational methodology is valid and effective to treat the macro-scale dynamics of the two-phase cavitating flow. Especially, the compressible Navier–Stokes equations for the mixture fluid allow to use a high-order numerical scheme (with selective filtering), to resolve not only the transient characteristics of the complex two-phase flow physics (e.g. formation, detachment, convection, and collapse of the cavitation bubble clouds) but also the generation and propagation of the linear and non-linear waves in the entire field. The direct numerical simulation of the cavitating flows noise from a 2D circular cylinder shows that, at cavitation numbers $\sigma = 1$ and 0.7, the shock waves generated by the coherent collapse of cloud cavitation in the wake significantly change the aerodynamics and aerodynamic noise, including alteration of the Karman vortex shedding frequency. The present direct simulation results are verified by an acoustic analogy composed of monopole and dipole sources. The monopole source is modeled for the collapse of cavitation bubble cloud, based on a classical theory of Fitzpatrik and Strasberg and the dipole source is for the pressure fluctuations along the cylinder surface by shock wave reflections. The far-field noise predicted by direct simulation is in excellent agreement with that of acoustic analogy, and it also confirms the f^{-2} decaying rate in the spectrum, as predicted by the model of Fitzpatrik and Strasberg with the Rayleigh–Plesset equation.

References

[1] H. Soyama, H. Kato, R. Oba, Cavitation observation of severely erosive vortex cavitation arising in a centrifugal pump, Proceedings of the Third IMechE International Conference on Cavitation (1992) 103–110.
[2] G.E. Reisman, E.A. McKenney, C.E. Brennen, Cloud cavitation on an oscillating hydrofoil, Proceedings of the 20th ONR Symposium on Naval Hydrodynamics (1994) 328–340.
[3] M. Levy, M. Kjeldsen, R.E.A. Arndt, Cloud cavitation noise, in: APS, 53rd Annual Meeting of the Division of Fluid Dynamics, 2000.
[4] H.M. Fitzpatrick, M. Strasberg, Hydrodynamic source of sound, Proceedings of First ONR Symposium on Naval Hydrodynamics (1956) 241–281.
[5] G.F. Oweis, J. Choi, S.L. Ceccio, Dynamics and noise emission of laser induced cavitation bubbles in a vortical flow field, Journal of Acoustical Society of America 115 (3) (2004) 1049–1058.
[6] Y.C. Wang, C.E. Brennen, The noise generated by the collapse of a cloud of cavitation bubbles, ASME/JSME Symposium on Cavitation and Gas–liquid Flows in Fluid Machinery and Devices, FED 226 (1995) 17–29.
[7] Y.C. Wang, C.E. Brennen, Numerical computation of shock waves in spherical cloud of cavitation bubbles, ASME Journal of Fluid Engineering 121 (4) (1999) 872–880.
[8] T. Colonius, F. d'Auria, C.E. Brennen, Acoustic saturation in bubbly cavitating flow adjacent to an oscillating wall, Physics of Fluids 12 (2000) 2752–2761.
[9] L. van Wijngaarden, On the collective collapse of a large number of gas bubbles in water, Proceedings of the 11th International Conference on Applied Mechanics (1964) 854–861.
[10] Y. Chen, S.D. Heister, A numerical treatment for attached cavitation, ASME Journal of Fluids Engineering 116 (1994) 613–618.
[11] G.H. Schner, K. Lanzenberger, Vapor/liquid interfaces in cavitating flows, ASME, Cavitation and Multiphase Flow (1995) 17–22.
[12] M. Deshpande, J. Feng, C.L. Merkle, Numerical modeling of the thermodynamic effects of cavitation, Journal of Fluids Engineering 119 (1997) 420–427.
[13] Y. Delannoy, J.L. Kueny, Cavity flow predictions based on the Euler equations, ASME Cavitation and Multi-Phase Flow Forum 109 (1990).
[14] Y. Chen, S.D. Heister, Modeling hydrodynamic nonequilibrium in cavitating flows, ASME, Journal of Fluids Engineering 118 (1996) 172–178.
[15] Y. Ventikos, G. Tzabiras, A numerical method for the simulation of steady and unsteady cavitating flows, Computers and Fluids 29 (2000) 63–88.
[16] J.R. Edwards, R.K. Franklin, M.S. Liou, Low-diffusion flux-splitting methods for real fluid flow with phase transitions, AIAA Journal 38 (9) (2000) 1624–1633.
[17] A. Kubota, H. Kato, H. Yamaguchi, A new modeling of cavitating flows: a numerical study of unsteady cavitation on a hydrofoil section, Journal of Fluid Mechanics 240 (1992) 59–96.
[18] A.K. Singhal, N. Vaidya, A.D. Leonard, Multi-dimensional simulation of cavitating flows using a PDF model for phase change, in: ASME Fluids Engineering Division Summer Meeting, ASME Paper FEDSM97-3272, 1997.
[19] R.F. Kunz, D.A. Boger, D.R. Stinebring, T.S. Chyczewski, J.W. Lindau, H.J. Gibeling, S. Venkateswarn, T.R. Govindan, A preconditioned Navier–Stokes method for two-phase flows with application to cavitation prediction, Computers and Fluids 29 (2000) 849–875.
[20] I. Senocak, W. Shyy, A pressure-based method for turbulent cavitating flow computations, Journal of Computational Physics 176 (2002) 363–383.

[21] B.R. Shin, Y. Iwata, T. Ikohagi, Numerical simulation of unsteady cavitating flows using a homogenous equilibrium model, Computational Mechanics 30 (2003) 388–395.
[22] G.S. Jiang, C.W. Shu, Efficient implementation of weighted ENO schemes, Journal of Computational Physics 126 (1996) 202–228.
[23] Y. Ren, M. Liu, H. Zhang, A characteristic-wise hybrid compact-WENO scheme for solving hyperbolic conservation laws, Journal of Computational Physics 192 (2003) 365–386.
[24] S.K. Lele, Compact finite difference schemes with spectral-like resolution, Journal of Computational Physics 103 (1992) 16–42.
[25] D. Gaitonde, J.S. Shang, J.L. Young, Practical aspects of higher-order accurate finite volume schemes for wave propagation phenomena, International Journal for Numerical Methods in Engineering 45 (1999) 1849–1869.
[26] H.T. Chen, R. Collins, Shock wave propagation past on ocean surface, Journal of Computational Physics 7 (1971) 89–101.
[27] K. Akagawa, Gas–liquid Two-phase Flow, Corona Pub., Tokyo, 1974.
[28] D.R.H. Beattie, P.B. Whalley, A simple two-phase fractional pressure drop calculation method, International Journal of Multiphase Flow 8 (1982) 83–87.
[29] M.R. Visbal, D.V. Gaitonde, High-order-accurate methods for complex unsteady subsonic flows, AIAA Journal 37 (10) (1999) 1231–1239.
[30] N.B. Edgar, M.R. Visbal, A general buffer zone type non-reflecting boundary condition for computational aeroacoustics, AIAA-Paper 2003-3300, 2003.
[31] A. Harten, High-resolution schemes for hyperbolic conservation laws, Journal of Computational Physics 49 (1983) 260–278.
[32] A.D. Pierce, Acoustics, Acoustical Society of America, New York, 1989.
[33] C.H.K. Williamson, Vortex dynamics in the cylinder wake, Annual Review of Fluid Mechanics 28 (1996) 477–539.
[34] C.-Y. Wen, C.-L. Yeh, M.-J. Wang, C.-Y. Lin, On the drag of two-dimensional flow about a circular cylinder, Physics of Fluids 16 (2004) 3828–3831.
[35] R.D. Henderson, Details of the drag curve near the onset of vortex shedding, Physics of Fluids 7 (1995) 2102–2104.
[36] S.A. Fry, Investigating cavity/wake dynamics for a circular cylinder by measuring noise spectra, Journal of Fluid Mechanics 142 (1984) 187–200.
[37] Y. Saito, K. Sato, Cavitation bubble collapse and impact in the wake of a circular cylinder, in: Proceedings of the Fifth International Symposium on Cavitation (CAV2003), Cav03-GS-11-004, 2003.
[38] B.C. Syamala Rao, D.V. Chandrasekhara, K. Seetharamiah, A high-speed photographic study of vortex shedding behind circular cylinders of cavitating flows, Proceedings of 2nd International JSME Symposium Fluid Machinery and Fluidics (1972) 293–302.
[39] J.J. Varga, G. Sebestyen, Determination of the frequencies of wakes shedding from circular cylinders, Acta Technology 53 (1996) 91–108.
[40] P. Ausoni, M. Farhat, X. Escaler, E. Equsquiza, F. Avellan, Cavitation influence on von Karman vortex shedding and induced hydrofoil vibrations, Journal of Fluids Engineering 129 (8) (2007) 966–973.
[41] W.K. Blake, Mechanics of Flow Induced Sound and Vibration, Academic Press, 1986.
[42] C.E. Brennen, Cavitation and Bubble Dynamics, Oxford University Press, New York, 1995.
[43] S.L. Ceccio, C.E. Brennen, Observations of the dynamics and acoustics of travelling bubble cavitation, Journal of Fluid Mechanics 233 (1991) 633–660.